Dalton Transactions

PAPER

Cite this: *Dalton Trans.*, 2015, **44**, 2311

Structural, Raman spectroscopic and microwave dielectric studies on $Ni_{1-x}(Zn_{1/2}Zr_{1/2})_xW_{1-x}Nb_xO_4$ ceramic compounds with wolframite structure

S. D. Ramarao and V. R. K. Murthy*

Received 4th August 2014,
Accepted 5th December 2014

DOI: 10.1039/c4dt02364a

www.rsc.org/dalton

$Ni_{1-x}(Zn_{1/2}Zr_{1/2})_xW_{1-x}Nb_xO_4$ (x = 0.0–1.0) compositions were synthesized *via* conventional solid-state reaction method. Structural and lattice vibrational characteristics of these compositions were studied with the help of powder X-ray diffraction and Raman spectroscopic measurements. Rietveld refinements confirm the formation of all these compositions in monoclinic wolframite structure with *P*2/*c* space group. When moving towards Ni^{2+}-poor compositions, splitting in the X-ray reflections was observed and is explained with lattice parameter variation. With increasing value of x, Raman spectra show two additional Raman active modes and the possible reasons for observing these modes are discussed in terms of electronegativity difference of the randomly distributed cations in B-site of these compositions. X-ray photoelectron spectroscopic measurements were done to understand the chemical bonding states of different elements in these compositions. Surface morphology studies reveal that the average grain size increases with increasing x. Microwave dielectric properties such as dielectric constant and quality factor were measured using Hakki–Coleman and reflection cavity techniques and enhancement in these values with x is correlated with intrinsic parameters such as polarizability and 3d electrons present in the constituent ions of these compositions. Temperature coefficient of resonant frequency was measured using an invar cavity attached to a programmable hot plate and is explained with B-site octahedral distortion of these compositions. Well dense $Ni_{1-x}(Zn_{1/2}Zr_{1/2})_xW_{1-x}Nb_xO_4$ (x = 0.0–1.0) compositions possess good microwave dielectric properties.

1. Introduction

Dielectric ceramics such as dielectric resonators (DRs) have attracted much attention in the rapid growth of mobile, satellite and radar technology because of their compact size and low-loss nature in comparison with metallic wave guides and coaxial lines and lead to device miniaturization.[1,2] These DRs are available with different shapes such as solid cylinder, circular, tubular, spherical and parallelepiped. But in general, one sees solid cylinder and circular DRs in microwave integrated circuits.[3] Storage of microwave energy at discrete frequencies through total internal reflection at the air-dielectric interface is the basic working principle of these DRs.[3] A DR with higher dielectric constant ($\varepsilon_r \sim 20$) reduces the size of microwave devices which is because the wavelength of electromagnetic waves in the dielectric material is inversely proportional to the square root of dielectric constant. Enhanced signal to noise ratio is achieved by these DRs because of their lower dielectric loss or higher quality factor (Q > 3000 at 10 GHz).[1–3] Atmospheric conditions such as temperature affect the resonant frequency of these DRs which in turn influences the performance of microwave devices. The usability of microwave devices at different atmospheric conditions can be increased by tuning the temperature coefficient of the resonant frequency of these DRs.[1–3] Perovskites (ABO_3), complex perovskites ($AA'BB'O_3$), cation-deficient perovskites ($A_nB_{n-1}O_{3n}$) and columbites (AB_2O_6) materials have been extensively studied as DRs for microwave device applications because of the flexibility for substitution of different cations in A- and B-sites for tuning the dielectric properties of these compounds.[4–7]

Recently, researchers have focused on microwave dielectric properties of $A^{+2}B^{+6}O_4$ (B: Mo and W) compounds because of their lower processing temperatures and the possibility of formulating these compounds in different crystallographic symmetries such as monoclinic wolframite and tetragonal scheelite structures.[8–10] More recently, Zhou *et al.* reported low temperature firing (*i.e.* below 850 °C) ceramics with ABO_4 stoichiometry.[11,12] In the scheelite structure, the rigid symmetric isolated BO_4 tetrahedra are connected to AO_8 dodecahedra by corner sharing whereas the A-site dodecahedra are connected

Microwave Laboratory, Department of Physics, Indian Institute of Technology Madras, Chennai – 600 036, India. E-mail: vrkm@physics.iitm.ac.in; Fax: +91-44-22570545; Tel: +91-44-22574859

via edge sharing. On the other hand, in the wolframite structure, both A- and B-site cations are connected to six oxygen atoms giving distorted AO_6 and BO_6 octahedra where the B-site octahedra are distorted more than the A-site octahedra.[13] These A-site and B-site octahedra share edges and form zigzag chains running along the *z* direction.[13] The ionic radius of A-site cations determines the formation of $A^{+2}B^{+6}O_4$ (B: Mo, W) compounds in either wolframite or scheelite structure.[13,14] Wolframite structure with *P*2/*c* space group can be obtained with substitution of divalent cations with lower ionic radius, *i.e.* $r_A \leq 0.77$ Å (Ni, Mg, Mn, Zn and Co), at the A-site, whereas the $A^{2+}B^{6+}O_4$ (B: Mo and W) compounds form in the scheelite structure with $I4_1/a$ space group when the A-site is occupied by larger ($r_A \geq 0.99$ Å) divalent cations such as Ca, Sr, Pb and Ba.[13,14]

Structure and microwave dielectric properties of AWO_4 (A: Mg, Zn, Mn, Ca, Sr and Ba) were reported by Yoon *et al.* where they observed higher dielectric constant values for AWO_4 (A: Mg, Zn and Mn) in spite of their lower polarizability in comparison with AWO_4 (A: Ca, Sr and Ba) compounds which was attributed to the higher molar volume of wolframite structure than scheelite structure.[15] Puller *et al.* reported the microwave dielectric properties of AWO_4 (A: Mg, Zn, Ni and Co) compounds with wolframite structure and explained the variation in dielectric constant and quality factor in terms of an extrinsic parameter density.[16] As the ionic polarizability of Mo was not reported by Shanon,[17] Choi *et al.* calculated the polarizability of Mo (3.28 $Å^3$) using least square refinement in conjunction with the Clausius–Mosotti equation and discussed the variation in temperature coefficient of resonant frequency (τ_f) of wolframite-structured $AMoO_4$ (A: Mg, Zn and Mn) with molar volume of these compounds.[18] As the octahedral distortion is indirectly related to the volume of the unit cell, Kim *et al.* explained the variation in τ_f with octahedral distortion in compounds with wolframite structure.[19] Kim *et al.* reported that the quality factor variation in ABO_4 compounds with scheelite structure was correlated with their packing fraction.[14] More recently, a similar interpretation between quality factor and packing fraction was reported by Kim *et al.* in wolframite-structured ABO_4 (A: Ni, Zn and Mg; B: Mo and W) compounds where $NiWO_4$ possesses lower quality factor in spite of its higher quality factor than other compounds and explained this by the presence of localized d electrons present in Ni^{2+} ($3d^8$).[20]

These reports give an idea for improving the dielectric properties of wolframite-structured compounds and motivated us to synthesize low dielectric loss materials by replacing Ni^{2+} with ions having empty or completely filled d orbitals, such as Zr^{4+} (d^0) and Zn^{2+} (d^{10}). In order to stabilize the wolframite structure throughout composition range, we have replaced W^{6+} with Nb^{5+} and synthesized $Ni_{1-x}(Zn_{1/2}Zr_{1/2})_xW_{1-x}Nb_xO_4$ (x = 0.0–1.0) compositions. In the present report we studied the structural, lattice vibrational and microwave dielectric properties of $Ni_{1-x}(Zn_{1/2}Zr_{1/2})_xW_{1-x}Nb_xO_4$ (x = 0.0–1.0) compositions. Rietveld refinement was performed on all these compositions to study the variation in the structural characteristics. Raman mode assignment was done for all these compositions and reasons for the appearance of two additional modes for these compositions are explained in terms of the electronegativity difference between the elements occupying the same site. According to the literature, $NiWO_4$ possess very low quality factor among the compounds with wolframite structure. Therefore, in the present paper we report the enhancement in the quality factor and dielectric constant with substitution of Zn^{2+}, Zr^{4+} at the A-site and Nb^{5+} at the B-site of $NiWO_4$ compound. The possible reasons for enhancement in the microwave dielectric properties of $Ni_{1-x}(Zn_{1/2}Zr_{1/2})_xW_{1-x}Nb_xO_4$ (x = 0.0–1.0) compositions are explained with reference to the intrinsic parameters such as polarizability, d electrons present in the constituent ions and B-site octahedral distortion of these compositions.

2. Experimental procedures

A conventional solid-state reaction method was followed for synthesizing the $Ni_{1-x}(Zn_{1/2}Zr_{1/2})_xW_{1-x}Nb_xO_4$ (x = 0.0–1.0) compositions. Initial ingredients NiO (99.9%), ZnO (99.95%), ZrO_2 (99.7%), WO_3 (99.95%) and Nb_2O_5 (99.5%) were weighed with stoichiometric amounts and were ground in an agate mortar using a pestle for 2 h. All the compositions were calcined in the 900–1300 °C temperature range with holding time of 4 h. Both heating and cooling were maintained at a rate of 5 °C min^{-1}. The obtained agglomerated powders were again ground in both dry and wet conditions in order to get fine powders. These fine powders were used for collecting the powder X-ray diffraction patterns of $Ni_{1-x}(Zn_{1/2}Zr_{1/2})_xW_{1-x}Nb_xO_4$ (x = 0.0–1.0) compositions using a Philips PANAlytical X'pert Pro X-ray diffractometer with X'Celerator detector. We used Cu K_α radiation at an acceleration condition of 40 kV and 30 mA. Both the incident and receiving Soller slits were maintained at 0.02° whereas the divergent slit was maintained at 1° and data were collected with a scan step of 0.0169°. Structural characteristics of $Ni_{1-x}(Zn_{1/2}Zr_{1/2})_xW_{1-x}Nb_xO_4$ (x = 0.0–1.0) compositions were studied with the help of Rietveld refinement using GSAS suite equipped with EXPGUI software.[21,22] The initial parameters for these refinements were taken from a report by Daturi *et al.*[13] Cylindrical pellets of 8 mm in diameter and 7 mm in thickness were prepared by adding 3 wt% polyvinyl alcohol to these powders. A uniaxial hydraulic press with a pressure of 200 MPa was used for this compaction process. All these pellets were placed on a platinum foil and sintered in the 1200–1350 °C temperature range using a conventional resistive heating furnace.

A Horiba Jobin Yvon HR800 UV Raman spectrometer equipped with a Peltier-cooled charge-coupled device detector was used to collect Raman spectra of polished and thermally etched $Ni_{1-x}(Zn_{1/2}Zr_{1/2})_xW_{1-x}Nb_xO_4$ (x = 0.0–1.0) compositions. All these measurements were done with a He-Ne laser source with an excitation wavelength λ = 632.8 nm and the measured output power at the surface of the sample was about 3 mW. Chemical bonding states of the constituent elements of the compositions were determined using X-ray photoelectron spectroscopy (XPS, Omicron Nanotechnology) measurements.

The bulk densities of all the sintered compositions were measured using the Archimedes technique. Surface morphology of polished and thermally etched compositions was studied with the help of an FEI Quanta 400 high-resolution scanning electron microscope. A Vector Network Analyzer (PNA-L N5230C) was used to measure the microwave dielectric properties of the compositions. Dielectric constant and quality factor of $Ni_{1-x}(Zn_{1/2}Zr_{1/2})_xW_{1-x}Nb_xO_4$ (x = 0.0–1.0) compositions were measured using the Hakki–Coleman method[23] and reflection technique whereas the temperature coefficient of resonant frequency (τ_f) of all the compositions was calculated using the following formula:

$$\tau_f = \frac{f_{85} - f_{25}}{f_{25} \times (85 - 25)} \text{ ppm } ^\circ C^{-1} \quad (1)$$

where f_{85} and f_{25} are the resonant frequencies at 85 °C and 25 °C respectively.

AC conductivities of $Ni_{1-x}(Zn_{1/2}Zr_{1/2})_xW_{1-x}Nb_xO_4$ (x = 0.0–1.0) compositions were measured at room temperature using an LCR meter (PSM 1700 N4L).

3. Results and discussion

3.1 Structural and spectroscopic studies

X-ray diffraction patterns of $Ni_{1-x}(Zn_{1/2}Zr_{1/2})_xW_{1-x}Nb_xO_4$ (x = 0.0–1.0) compositions are shown in Fig. 1. We can clearly see that all the X-ray reflections are shifted to lower angle with increasing value of x. Substitution of higher ionic radius[24] elements Zn^{2+} (0.74 Å), Zr^{4+} (0.72 Å) and Nb^{5+} (0.64 Å) ions in place of lower ionic radius elements Ni^{2+} (0.69 Å) and W^{6+} (0.62 Å) increases the unit cell volume from 128.05 $Å^3$ to 138.68 $Å^3$ which in turn causes the reflections to shift towards lower angle. In addition to this shifting, we observed a splitting in X-ray reflections which is clearly seen in Fig. 1. In order to understand the splitting in the X-ray reflections, we plotted

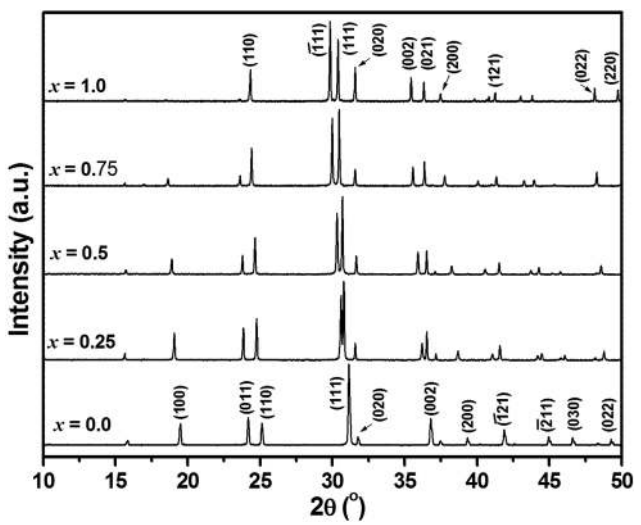

Fig. 1 Powder X-ray diffractions patterns of $Ni_{1-x}(Zn_{1/2}Zr_{1/2})_xW_{1-x}Nb_xO_4$ compositions.

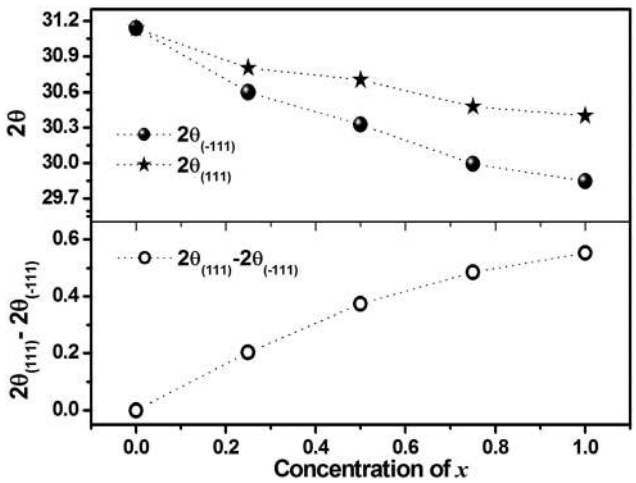

Fig. 2 Variation of 2θ values of (−111) and (111) reflections and their difference as a function of x.

the 2θ values of (−111) and (111) reflections as a function of composition as shown in Fig. 2. The difference in 2θ values of these reflections is shown in the same plot (*i.e.* Fig. 2). This splitting may be due to any phase transition or changes in the lattice parameters with increasing value of x in these compositions. Rietveld refinement was performed on all these compositions and observed to fit well with the $P2/c$ space group and confirms the formation of all these compositions in monoclinic wolframite structure. Refinement plots of all the compositions are shown in Fig. 3(a–e) and the structural (lattice) parameters are given in Table 1 and Wyckoff positions and occupancies of x = 0.5 composition are given in Table 2. Fig. 4 and 5 show the variation of lattice parameters of $Ni_{1-x}(Zn_{1/2}Zr_{1/2})_xW_{1-x}Nb_xO_4$ (x = 0.0–1.0) compositions. We do not observe much difference in lattice parameters (a, b and c) in spite of the substitution of higher ionic radius elements in place of lower ionic radius elements, whereas the monoclinic angle β shows an increase from 90.05° to 91.73°. As $Ni_{1-x}(Zn_{1/2}Zr_{1/2})_xW_{1-x}Nb_xO_4$ (x = 0.0–1.0) compositions possess monoclinic wolframite structure, the splitting in X-ray reflections is explained by the variation in lattice parameters of these compositions. The d-spacing values of maximum intensity (−111) and (111) reflections of all these compositions were calculated using the obtained lattice parameters from Rietveld refinement and the following formula and are given in Table 3:

$$\frac{1}{d_{(hkl)}^2} = \frac{1}{\sin^2\beta}\left[\frac{h^2}{a^2} + \frac{k^2\sin^2\theta}{b^2} + \frac{l^2}{c^2} - \frac{2hl\cos\beta}{ac}\right] \quad (2)$$

where h, k and l represent the indices of the corresponding reflection, and a, b, c and β represent the lattice parameters of the respective compositions.

Fig. 6 shows the variation of $[d_{(-111)}-d_{(111)}]$ with increasing value of x. It is clearly understood from Fig. 6 that an increase in the lattice parameters enhances the difference in the d-spacing of (−111) and (111) reflections and is responsible for the splitting in X-ray reflections of all these compounds. Here,

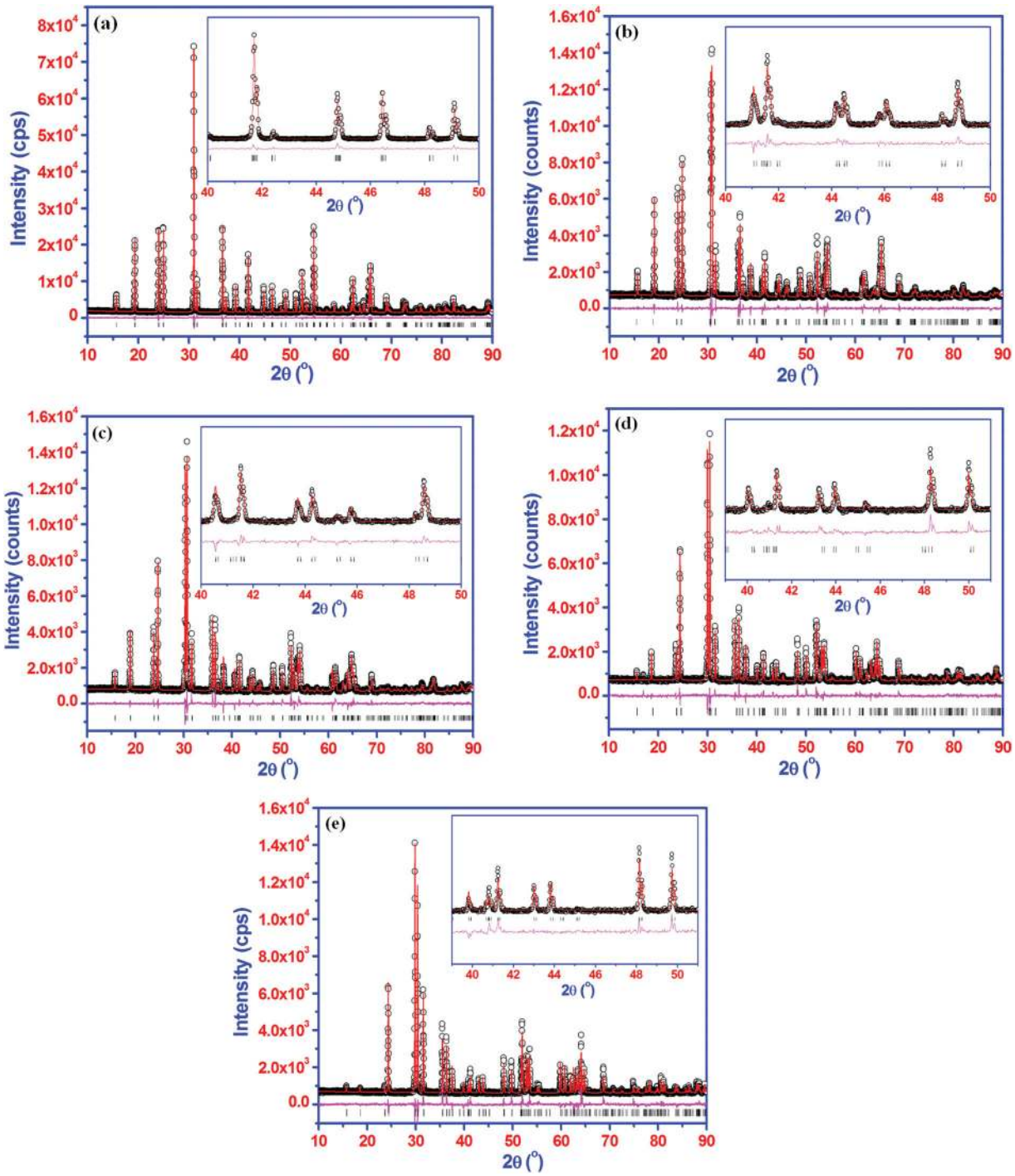

Fig. 3 Rietveld refinement plots of (a) x = 0.0, (b) x = 0.25, (c) x = 0.50, (d) x = 0.75 and (e) x = 1.0 compositions. (Observed powder X-ray diffraction data (o), calculated diffraction pattern with red solid line and difference plot with magenta line.)

we have calculated d-spacing values for maximum intensity reflections and a similar analysis can also be extended to explain the splitting of other reflections on the higher angle side. In the case of x = 0 composition, we have not seen splitting in maximum intensity reflection in spite of very low value of $[d_{(-111)}$–$d_{(111)}]$, *i.e.* 0.0018 Å. This might be because of the use of a higher scan step size (0.0169°) for all these measurements. We have not investigated this further by decreasing the scan step size because our instrument's minimum scan step size limit (0.004°) is higher than the required one. Hence, this splitting in the X-ray reflections of all the compositions is explained by lattice parameter variation.

Fig. 7 shows the crystal structure of $NiWO_4$ composition. Both Ni^{2+} and W^{6+} are connected with six oxygen atoms

Table 1 Lattice parameters (*a*, *b*, *c* and *β*) of $Ni_{1-x}(Zn_{1/2}Zr_{1/2})_xW_{1-x}Nb_xO_4$ compositions

x	*a* (Å)	*b* (Å)	*c* (Å)	*β* (°)
0.0	4.600	5.666	4.912	90.05
0.25	4.655	5.664	4.963	90.49
0.5	4.714	5.662	5.01	90.94
0.75	4.766	5.665	5.048	91.23
1.0	4.805	5.673	5.082	91.71

Table 2 Wyckoff positions and occupancies of *x* = 0.5 composition

Atom	*x*	*y*	*z*	Occupancy
Ni	0.5	0.678(4)	0.25	0.50
Zn	0.5	0.678(4)	0.25	0.25
Zr	0.5	0.678(4)	0.25	0.25
W	0	0.177(2)	0.25	0.50
Nb	0	0.177(2)	0.25	0.50
O1	0.226(1)	0.126(8)	0.917(2)	1.0
O2	0.272(2)	0.379(3)	0.383(2)	1.0

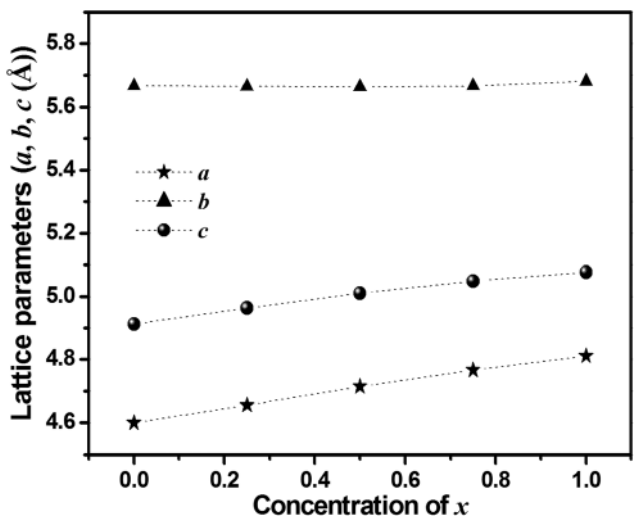

Fig. 4 Lattice parameters (*a*, *b* and *c*) of $Ni_{1-x}(Zn_{1/2}Zr_{1/2})_xW_{1-x}Nb_xO_4$ compositions.

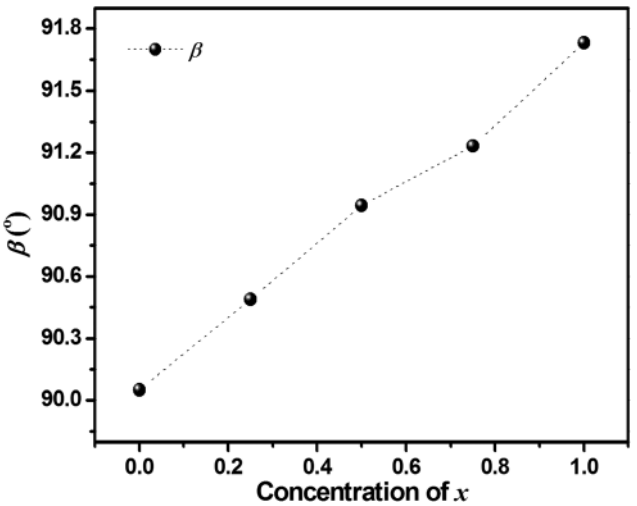

Fig. 5 Monoclinic angle (*β*) of $Ni_{1-x}(Zn_{1/2}Zr_{1/2})_xW_{1-x}Nb_xO_4$ compositions.

Table 3 Calculated *d*-spacing values of $Ni_{1-x}(Zn_{1/2}Zr_{1/2})_xW_{1-x}Nb_xO_4$ compositions

x	$d_{(-111)}$ (Å)	$d_{(111)}$ (Å)	$d_{(-111)}$–$d_{(111)}$ (Å)
0.0	2.88836	2.88651	0.00185
0.25	2.92023	2.90195	0.01828
0.50	2.95232	2.91717	0.03515
0.75	2.97845	2.93235	0.04610
1.0	3.00667	2.94157	0.06510

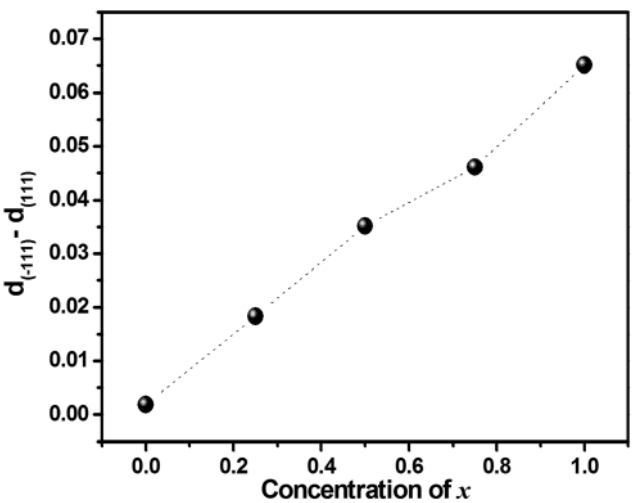

Fig. 6 Variation of $d_{(-111)}$–$d_{(111)}$ for $Ni_{1-x}(Zn_{1/2}Zr_{1/2})_xW_{1-x}Nb_xO_4$ solid solution.

forming distorted NiO_6 and WO_6 octahedra where the latter is more distorted than the former. B-site (W^{6+}) octahedra connect with other B-site (W^{6+}) octahedra by edge sharing and are extended along the *c*-axis and form a zigzag chain type arrangement. A similar arrangement is also observed for A-site (Ni^{2+}) octahedra. In the wolframite structure Ni^{2+} and W^{6+} occupy 2f and 2e Wyckoff positions respectively whereas the two distinguishable oxygen atoms occupy the same site, *i.e.* 4 g. Oxygen O1 is connected to one B-site (W^{6+}) with one short terminal bond and to two A-site (Ni^{2+}) cations with relatively longer bonds. On the other hand, oxygen O2 bridges two B-site (W^{6+}) cations and is connected to one A-site (Ni^{2+}) cation. With substitution of higher ionic radius elements (Zn^{2+}, Zr^{4+} and Nb^{5+}) in place of lower ionic radius elements (Ni^{2+} and W^{6+}), the cation–oxygen bond lengths are elongated or compressed. In the wolframite structure, B-site octahedra are distorted more and show an impact on the microwave dielectric pro-

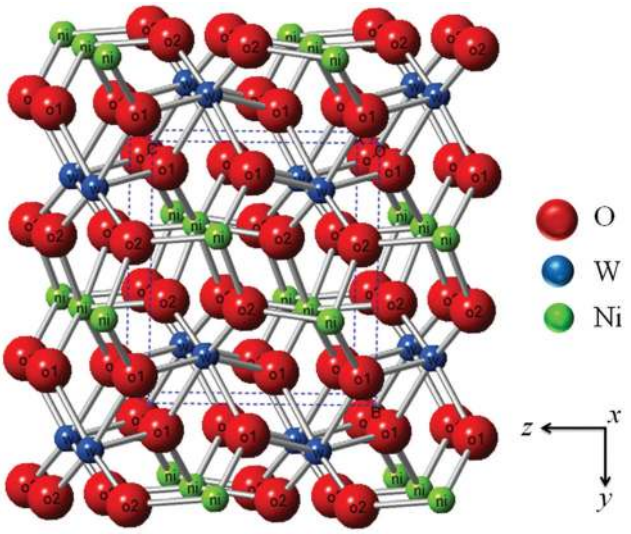

Fig. 7 Crystal structure of $NiWO_4$ composition.

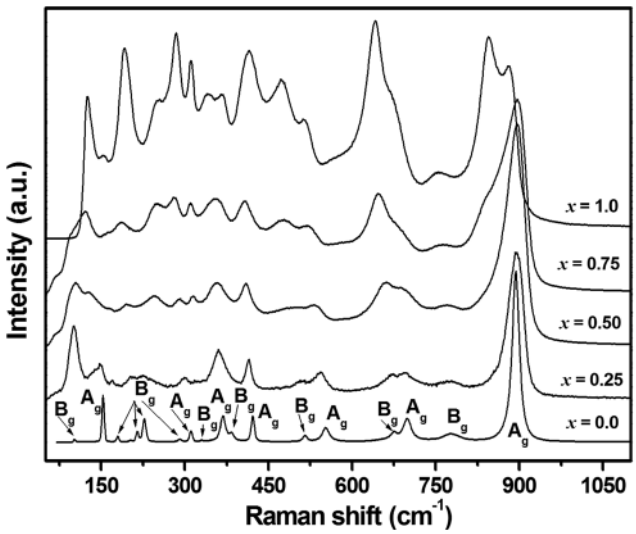

Fig. 8 Raman spectra of $Ni_{1-x}(Zn_{1/2}Zr_{1/2})_xW_{1-x}Nb_xO_4$ compositions.

perties of materials. Therefore, we have calculated B-site octahedral distortion of $Ni_{1-x}(Zn_{1/2}Zr_{1/2})_xW_{1-x}Nb_xO_4$ (x = 0.0–1.0) compositions using the obtained (Nb/W)–O bond length from Rietveld refinement and the following expression.[19] The calculated values are in the range of 10 to 20% and are given in Table 6.

$$\text{Octahedral distortion, } \delta(\%) = \frac{(\text{B–O distance}_{\text{largest}}) - (\text{B–O distance}_{\text{smallest}})}{\text{B–O distance}_{\text{average}}} \quad (3)$$

Raman spectroscopy is an important and widely used experimental technique to understand the structural and vibrational properties of different classes of materials. In general, the vibrational modes in ABO_4 compositions with wolframite crystal structure are grouped into internal and external modes where the former are associated with $[(B_2O_8)^{4-}]_n$ polymeric anion in which the B-site cation is covalently bonded with oxygen atoms.[13] The vibrational modes coming from A–O and lattice vibrations are grouped into external modes. Because of the higher covalent nature of B–O bonds, internal vibrational modes are observed at higher frequency whereas the external modes arising from A–O bonds will appear at lower frequency.[25,26] The effect of substitution of different cations (Zn^{2+}, Zr^{4+}) at A-sites and (Nb^{5+}) at B-sites of $NiWO_4$ compound was studied by collecting room temperature Raman spectra of $Ni_{1-x}(Zn_{1/2}Zr_{1/2})_xW_{1-x}Nb_xO_4$ (x = 0.0–1.0) compositions, which are shown in Fig. 8.

Group theoretical calculations predicted 36 vibrational modes for ABO_4 type compositions having the wolframite structure with $P2/c$ space group and the irreducible representation of all these modes is given below:[13]

$$\Gamma = 8A_g + 10B_g + 8A_u + 10B_u \quad (4)$$

where all the 'g' vibrations are Raman active whereas 'u' vibrations are IR active.

Fig. 8 shows the Raman spectra of $Ni_{1-x}(Zn_{1/2}Zr_{1/2})_xW_{1-x}Nb_xO_4$ (x = 0.0–1.0) solid solutions. For the x = 0 composition, we observe two Raman active modes in the high-frequency range (1000–750 cm^{-1}) where the higher intensity mode at 893 cm^{-1} is assigned to the symmetric vibrations of short W–O bonds as this frequency range is typical for symmetric vibrations of highly covalent bonds. The second mode at 776 cm^{-1} is assigned to the asymmetric vibrations of short W–O terminal bonds.[13] In the mid frequency range (750–500 cm^{-1}), four Raman modes were observed, of which two modes at 698.2 and 675.3 cm^{-1} are assigned to asymmetric stretching vibrations of W–O–W bridges whereas the two lower frequency modes are assigned to symmetric stretching vibrations of W–O–W bridges. The modes corresponding to in-plane vibrations of shorter and longer W–O bonds are observed in the 500–330 cm^{-1} frequency range, whereas the strong mode at 368.1 cm^{-1} is assigned to the symmetric vibrations of NiO_6 octahedra. The remaining Raman active modes below 350 cm^{-1} are assigned to the out-of-plane vibrations of W–O bonds and lattice vibrations in the wolframite crystal structure.[13] The complete assignment of room temperature Raman spectra of $Ni_{1-x}(Zn_{1/2}Zr_{1/2})_xW_{1-x}Nb_xO_4$ (x = 0.0–1.0) compositions is shown in Fig. 8.

The Raman spectra of $Ni_{1-x}(Zn_{1/2}Zr_{1/2})_xW_{1-x}Nb_xO_4$ (x = 0.0–1.0) solid solutions possess all the expected modes in accordance with the wolframite structure with $P2/c$ space group. As the Raman modes are very sensitive to the nature of bonding and distribution of cations at respective Wyckoff sites, substitutions of multiple cations (Zn^{2+}, Zr^{4+}) at Ni^{2+} sites and Nb^{5+} in place of W^{6+} show considerable changes in the Raman spectra of these compositions. Changes in the cation–oxygen bond lengths and masses of the constituent ions by substitution of multiple cations at A-sites and B-sites of $NiWO_4$ might be responsible for the shift in the Raman modes of

these compositions. The random distribution of (Zn^{2+}, Zr^{4+}) at Ni^{2+} sites and Nb^{5+} at W^{6+} sites is responsible for the change in the full width at half maximum (FWHM) and intensity of Raman active modes for all these compositions. Along with these changes, two more features were noticed in the Raman spectra of these compositions. One is the splitting in the symmetric stretching mode at 893 cm^{-1} and the other is an additional mode appearing around 600 cm^{-1}. As the mode at 893 cm^{-1} corresponds to the symmetric stretching vibrations of B–O bonds, splitting of this mode might be due to the electronegativity difference between Nb (1.6) and W (2.36) atoms present at the same site.[13] The lower electronegativity of Nb results in the formation of highly covalent bonds with oxygen in comparison with W–O bonds. In general, longer dimensional range associated with diffraction phenomena restricts the prediction of the variation in the local bonding characteristics through powder X-ray diffraction measurements. Therefore, we have not observed any difference in the powder diffractograms of these compositions. On the other hand, Raman spectroscopy is very sensitive to the distribution of cations at different sites which allows us to differentiate randomly distributed Nb^{5+} and W^{6+} ions in the present $Ni_{1-x}(Zn_{1/2}Zr_{1/2})_xW_{1-x}Nb_xO_4$ (x = 0.0–1.0) solid solutions. Raman spectra of all these compositions ($x \geq 0.25$) were deconvoluted and are shown in Fig. 9. It is clearly seen from these figures that the splitting in the strongest Raman mode (A_g mode at 893 cm^{-1}) and the intensity of the additional mode around 600 cm^{-1} increase with increasing value of x. The proposed assignment of all the modes of $Ni_{1-x}(Zn_{1/2}Zr_{1/2})_x$-$W_{1-x}Nb_xO_4$ (x = 0.0–1.0) compounds is given in Table 4.

In order to understand the chemical bonding characteristics of these compositions, we carried out X-ray photoelectron spectroscopy (XPS) measurements on $Ni_{1-x}(Zn_{1/2}Zr_{1/2})_x$-$W_{1-x}Nb_xO_4$ (x = 0.0, 0.25, 0.50 and 0.75) compositions. Fig. 10 shows the high-resolution XPS spectra of Ni (2p), W (4f) and O (1s). The binding energies of the corresponding elements are given in Table 5. It is clear that for all these compositions (*i.e.* x = 0.0, 0.25, 0.50 and 0.75), Ni ($2p_{3/2}$) has a binding energy in the range 861.5 to 866.5 eV and is in good agreement with the literature[27,28] for Ni^{2+}. On the other hand, the W 4f level shows an asymmetric profile in the case of x = 0.0 and 0.25 compositions and is deconvoluted into two (*i.e.* $4f_{7/2}$ and $4f_{5/2}$), whereas in the case of x = 0.50 and 0.75, these $4f_{7/2}$ and $4f_{5/2}$ are well separated and are consistent with an earlier report[29] on materials containing W^{6+}. This confirms that in all Ni_{1-x}-$(Zn_{1/2}Zr_{1/2})_xW_{1-x}Nb_xO_4$ (x = 0.0, 0.25, 0.5 and 0.75) compositions both Ni and W elements are in +2 and +6 oxidation states respectively. Fig. 10 indicates that the O (1s) level has an asymmetric shape which is deconvoluted into two. Of these, the energy level in the range 533–535 eV is assigned to the O (1s) level and the other level around 537 eV may be assigned to the surface defect form in these compositions.[30] Binding energy values of O (1s) for all these compositions are given in Table 5. The 2p core level spectra of Zn are shown in Fig. 11.

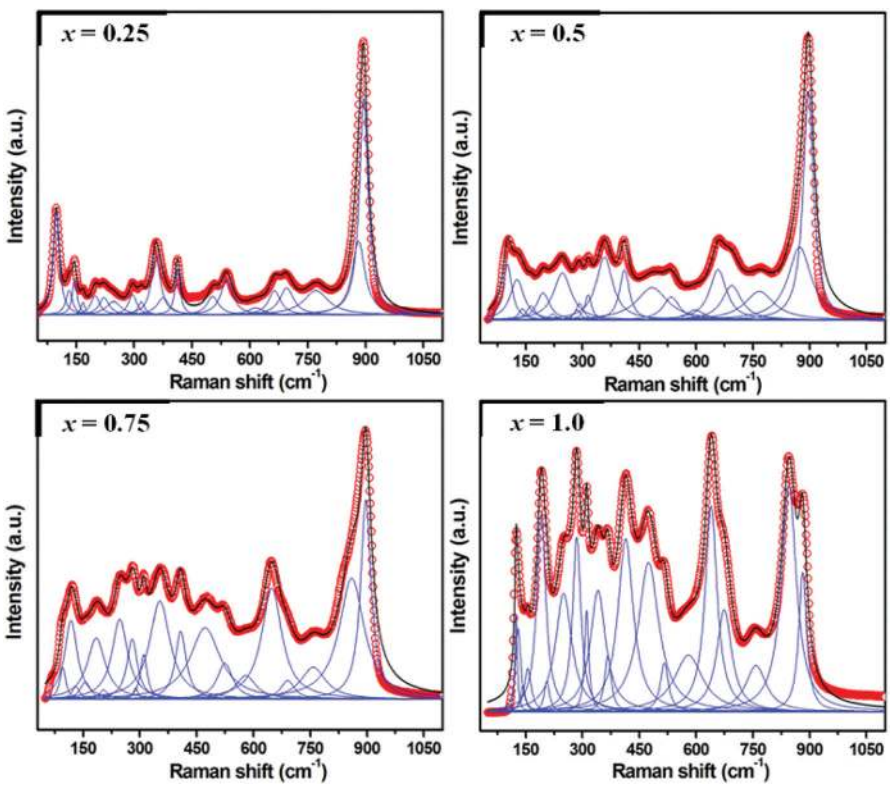

Fig. 9 Deconvoluted Raman spectra of $Ni_{1-x}(Zn_{1/2}Zr_{1/2})_xW_{1-x}Nb_xO_4$ compositions.

Table 4 Proposed Raman mode assignments for $Ni_{1-x}(Zn_{1/2}Zr_{1/2})_xW_{1-x}Nb_xO_4$ compositions with wolframite structure

Symmetry	x = 0.0	x = 0.25	x = 0.50	x = 0.75	x = 1.0
A_g	893.0	895.9 (878.9)	896.5 (873.5)	896.8 (859.5)	881.6 (853.2)
B_g	776.0	776.2	767.4	758.1	756.9
A_g	698.2	696.9	694.7	678.9	674.9
B_g	675.3	666.1	657.7	645.4	640.9
—	—	615.3	598.4	580.0	585.7
A_g	552.7	543.1	534.2	525.8	517.1
B_g	515.2	507.2	483.8	473.7	474.0
A_g	421.3	412.5	410.6	408.7	413.2
B_g	383.5	379.9	357.7	356.6	367.5
A_g	368.1	360.6	315.2	310.7	340.8
B_g	330.4	322.6	292.5	288.8	311.0
A_g	311.0	298.9	286.1	279.7	284.8
B_g	291.0	263.0	247.3	246.2	249.3
A_g	227.2	226.5	221.1	204.2	205.8
B_g	214.4	203.3	194.6	184.7	190.9
B_g	202.5	170.6	161.9	155.8	155.3
B_g	179.7	148.6	142.0	130.6	142.4
A_g	153.3	133.9	126.9	117.9	129.9
B_g	101.8	101.1	101.5	96.0	124.3

We can clearly see from this figure that there are two binding energy levels around 1026 eV and 1049 eV which are consistent with the literature.[31,32] The lower binding energy level at 1026 eV is assigned to the core $2p_{3/2}$ level whereas the other is assigned to $2p_{1/2}$; the binding energy values of these levels for all the compositions are given in Table 5. Boyuklimanli *et al.* reported that the $3d_{5/2}$ core level of Zr was observed around 185.3 eV. Recently, a similar finding was reported by Dong *et al.*[33,34] In our present study on $Ni_{1-x}(Zn_{1/2}Zr_{1/2})_xW_{1-x}Nb_xO_4$ (x = 0.25, 0.5 and 0.75) compositions, we observed two spectral lines around 186 eV and 189 eV and these are assigned to 3d core levels of Zr element, *i.e.* $3d_{5/2}$ and $3d_{3/2}$ respectively. In our present studies, we have observed a doublet around 211 eV. It was reported[35] that the $3d_{5/2}$ of Nb was observed around 208.2 eV. Hence, the spectral line observed at 211 eV is assigned to the $3d_{5/2}$ spectral line of Nb element present in all these compositions whereas the higher binding energy spectral line (*i.e.* 214 eV) is assigned to $3d_{3/2}$ of Nb. The binding energy values of spectral lines of the constituent elements of $Ni_{1-x}(Zn_{1/2}Zr_{1/2})_xW_{1-x}Nb_xO_4$ (x = 0.0, 0.25, 0.5 and 0.75) compositions are given in Table 5.

3.2 Density and microstructural studies

The Archimedes technique was used to measure the bulk densities of $Ni_{1-x}(Zn_{1/2}Zr_{1/2})_xW_{1-x}Nb_xO_4$ (x = 0.0–1.0) compositions with an accuracy of ± 0.005 and they are given in

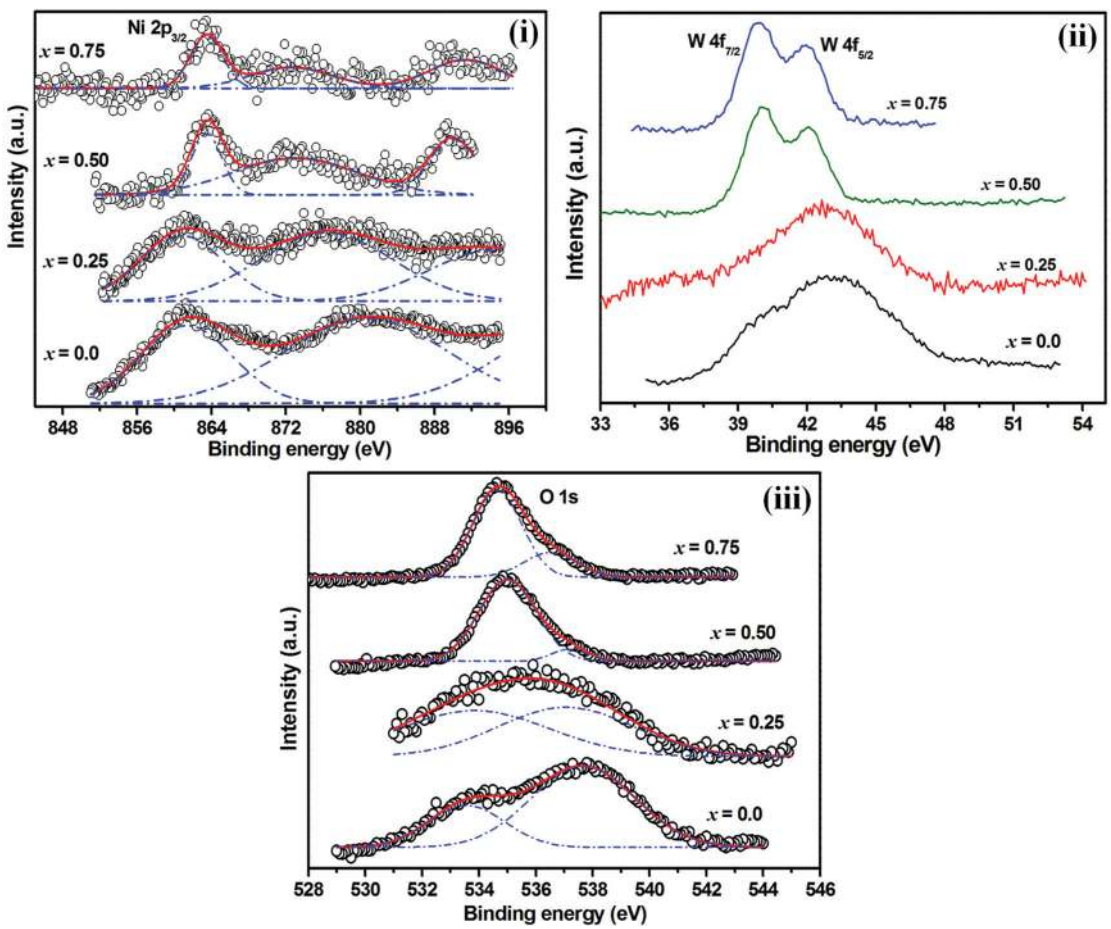

Fig. 10 High-resolution XPS spectra of (i) Ni (2p), (ii) W (4f) and (iii) O (1s) core levels in $Ni_{1-x}(Zn_{1/2}Zr_{1/2})_xW_{1-x}Nb_xO_4$ compositions.

Table 5 Binding energies of constituent elements of $Ni_{1-x}(Zn_{1/2}Zr_{1/2})_xW_{1-x}Nb_xO_4$ (x = 0.0, 0.25, 0.50 and 0.75) compositions

Element	Spectral line	x = 0.0	x = 0.25	x = 0.50	x = 0.75
Ni	$2p_{3/2}$	861.2 (±0.15)	861.5 (±0.23)	862.4 (±0.04)	866.5 (±0.15)
W	$4f_{7/2}$	39.7 (±0.09)	39.4 (±0.13)	39.9 (±0.12)	39.8 (±0.14)
	$4f_{5/2}$	43.2 (±0.06)	42.9 (±0.15)	42.2 (±0.15)	41.9 (±0.12)
O	1s	533.5 (±0.07)	533.8 (±0.05)	534.8 (±0.06)	534.6 (±0.04)
Zn	$2p_{3/2}$	—	1026.2 (±0.07)	1026.4 (±0.03)	1026.1 (±0.08)
	$2p_{1/2}$	—	1049.2 (±0.04)	1049.6 (±0.09)	1049.3 (±0.03)
Zr	$3d_{5/2}$	—	187.2 (±0.09)	186.8 (±0.08)	186.6 (±0.05)
	$3d_{3/2}$	—	189.6 (±0.05)	189.1 (±0.04)	188.9 (±0.03)
Nb	$3d_{5/2}$	—	213.2 (±0.08)	211.3 (±0.06)	211.4 (±0.07)
	$3d_{3/2}$	—	215.3 (±0.03)	214.0 (±0.07)	214.1 (±0.08)

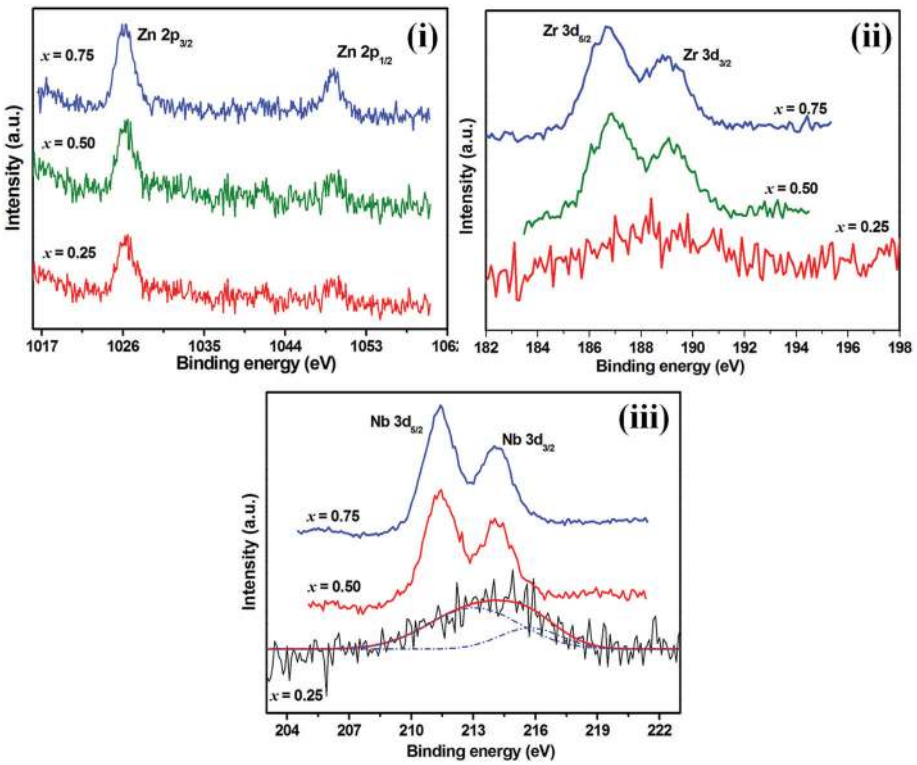

Fig. 11 High-resolution XPS spectra of (i) Zn (2p), (ii) Zr (3d) and (iii) Nb (3d) core levels in $Ni_{1-x}(Zn_{1/2}Zr_{1/2})_xW_{1-x}Nb_xO_4$ compositions.

Table 6. The theoretical densities of all these compounds were calculated using the following formula:

$$\rho_{th} = \frac{nM}{NV}\ g\ cm^{-3} \quad (5)$$

where n and M give the number of formula units per unit cell and molecular weight of the samples respectively and N and V represent the Avogadro number (6.022×10^{23} mol^{-1}) and molar volume of the samples respectively. The molar volume (V_m) of all these compounds was calculated using the data obtained from Rietveld refinement. Percentage of theoretical density of all these compounds was calculated using the measured density (ρ_m) and calculated theoretical density (ρ_{th}) and the following formula:

$$\rho\,(\%) = \frac{\rho_m}{\rho_{th}} \times 100 \quad (6)$$

All the $Ni_{1-x}(Zn_{1/2}Zr_{1/2})_xW_{1-x}Nb_xO_4$ (x = 0.0–1.0) compounds possess more than 95% of theoretical density and the values are given in Table 6.

An FEI Quanta 400 high-resolution scanning electron microscope was used to investigate the surface morphology of all the compositions. In order to get better micrographs, highly polished and thermally etched pellets were used for these measurements. Fig. 12(a–e) show the surface

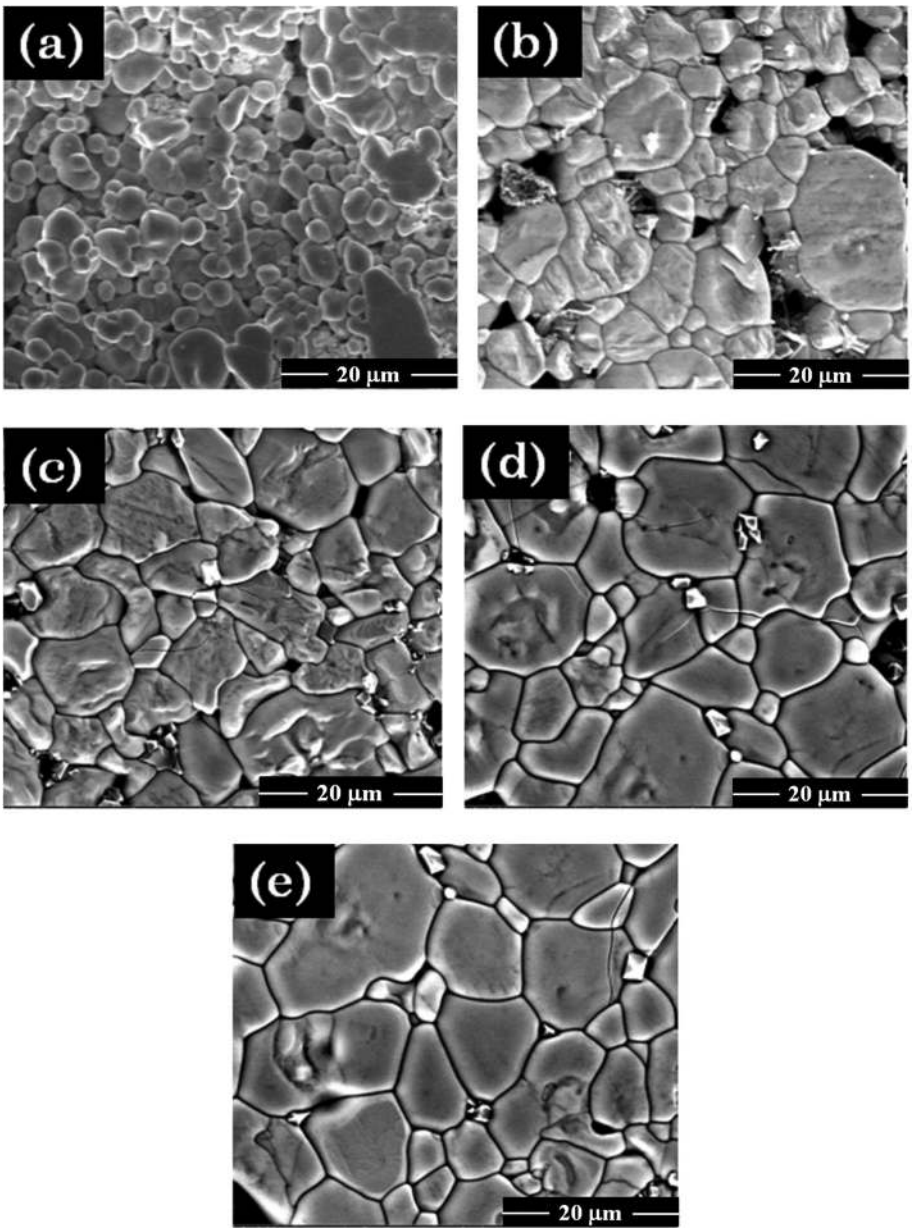

Fig. 12 Scanning electron micrographs of $Ni_{1-x}(Zn_{1/2}Zr_{1/2})_xW_{1-x}Nb_xO_4$ compositions: (a) x = 0.0 sintered at 1200 °C, (b) x = 0.25 sintered at 1250 °C, (c) x = 0.50 sintered at 1275 °C, (d) x = 0.75 sintered at 1275 °C and (e) x = 1.0 sintered at 1300 °C.

morphology of $Ni_{1-x}(Zn_{1/2}Zr_{1/2})_xW_{1-x}Nb_xO_4$ (x = 0.0–1.0) compositions. These micrographs reveal that grain size increases with increasing x.

3.3 Microwave dielectric characterization

Microwave dielectric properties such as dielectric constant, quality factor and temperature coefficient of resonant frequency of ceramic materials are influenced by extrinsic parameters such as secondary phases, porosity and density[36,37] which we can minimize by optimizing the processing conditions like calcination and sintering temperature of the materials. On the other hand, intrinsic parameters like ionic polarizability, molar volume, and structural characteristics also influence the microwave dielectric properties of ceramic materials.[38,39] In the present work, we have optimized the processing conditions like calcination temperature for obtaining single-phase compositions with wolframite structure and sintering temperature to achieve higher (≥95%) densification. Hence, we could succeed in minimizing the effect of extrinsic parameters on microwave dielectric properties of $Ni_{1-x}(Zn_{1/2}Zr_{1/2})_xW_{1-x}Nb_xO_4$ (x = 0.0–1.0) compositions. Therefore, in the present paper, we report the effect of structural parameters on dielectric properties of these compositions with wolframite structure.

3.3.1 Dielectric constant. The dielectric constant of $Ni_{1-x}(Zn_{1/2}Zr_{1/2})_xW_{1-x}Nb_xO_4$ (x = 0.0–1.0) compounds was measured

Table 6 Density (ρ), polarizability (α_D), dielectric constant (ε_r), quality factor ($Q \times f$), temperature coefficient of resonant frequency (τ_f), packing fraction (PF) and B-site octahedral distortion of $Ni_{1-x}(Zn_{1/2}Zr_{1/2})_xW_{1-x}Nb_xO_4$ compositions

x	ρ (%)	α_D (Å^3)	ε_r	$Q \times f$ (GHz)	τ_f (ppm °C^{-1})	PF (%)	δ (%)
0.0	95.2	12.470	12.4	23 400	−26.2	69.50	10.3
0.25	96.1	13.016	13.2	28 700	−29.1	68.29	15.6
0.50	96.7	13.562	14.8	32 650	−34.8	67.07	17.3
0.75	97.2	14.109	15.2	41 250	−44.7	65.86	18.7
1.0	97.8	14.655	16.2	53 350	−49.2	64.63	20.11

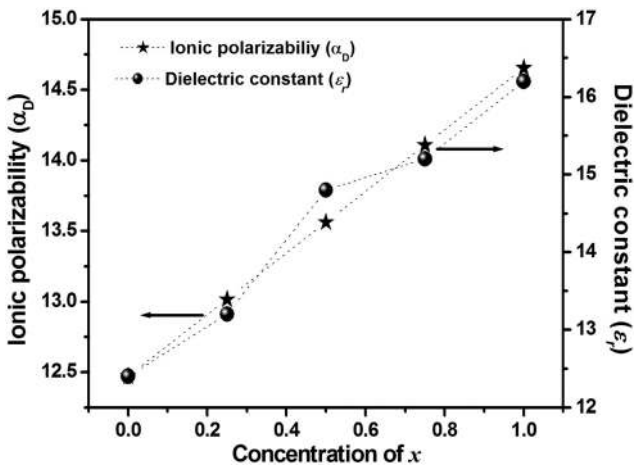

Fig. 13 Variation of dielectric constant and ionic polarizability of $Ni_{1-x}(Zn_{1/2}Zr_{1/2})_xW_{1-x}Nb_xO_4$ compositions.

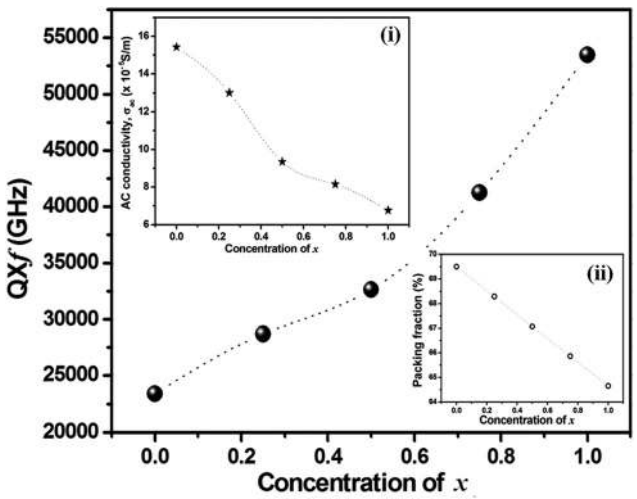

Fig. 14 Variation of quality factor of $Ni_{1-x}(Zn_{1/2}Zr_{1/2})_xW_{1-x}Nb_xO_4$ compositions. (Insets show the variation in (i) AC conductivity and (ii) packing fraction of these compositions with increasing x.)

using the Hakki–Coleman method and values are given in Table 6. Fig. 13 shows the variation of dielectric constant of $Ni_{1-x}(Zn_{1/2}Zr_{1/2})_xW_{1-x}Nb_xO_4$ (x = 0.0–1.0) compositions from which we can see that dielectric constant increases with increasing x. In general, dielectric constant of ceramic materials depends on extrinsic parameters such as density, porosity and secondary phases[40] present in the compounds. In the present study, as all these compounds possess more than 95% theoretical density with low porosity and show single phase with wolframite crystal structure, the variation in the dielectric constant is explained by intrinsic parameters such as polarizability. Substitution of more highly polarizable Zn^{2+} (2.04 Å^3), Zr^{4+} (3.25 Å^3) ions at Ni^{2+} (1.23 Å^3) sites and Nb^{5+} (3.97 Å^3) in place of W^{6+} (3.20 Å^3) increases the polarizability of the compounds[17] which in turn increases the dielectric constant of the compounds. The polarizability of $Ni_{1-x}(Zn_{1/2}Zr_{1/2})_xW_{1-x}Nb_xO_4$ (x = 0.0–1.0) compounds is calculated using the Shannon additive rule[17] and values are given in Table 6:

$$\begin{aligned}\alpha_D(Ni_{1-x}(Zn_{1/2}Zr_{1/2})_xW_{1-x}Nb_xO_4) &= (1-x)\alpha_D(Ni^{2+}) + 0.5x\alpha_D(Zn^{2+}+Zr^{4+}) \\ &+ (1-x)\,\alpha_D(W^{6+}) + x\alpha_D(Nb^{5+}) + 4\alpha_D(O^{2-})\end{aligned} \quad (7)$$

3.3.2 Quality factor. The reflection cavity technique was used to measure the quality factor ($Q \times f$) of $Ni_{1-x}(Zn_{1/2}Zr_{1/2})_xW_{1-x}Nb_xO_4$ (x = 0.0–1.0) compounds and the values are given in Table 6. Fig. 14 shows the variation of quality factor of $Ni_{1-x}(Zn_{1/2}Zr_{1/2})_xW_{1-x}Nb_xO_4$ (x = 0.0–1.0) compositions and reveals that, with increasing x from 0.0 to 1.0, the quality factor gradually increases from 23 500 GHz to 53 450 GHz. It was reported that the quality factor of ceramic materials depends on porosity, density and secondary phases[16,40] present in the materials which can be minimized through optimization of processing conditions. Along with structural parameters such as bonding characteristics and packing fraction,[14] the nature of elements that are accommodated in the crystal structure[41] can also influence the quality factor of ceramic materials. Pullar *et al.* observed that the quality factor of AWO_4 (A: Mg, Zn, Ni and Co) compounds with wolframite structure depends on the extrinsic parameters such as density and microstructure of these compounds and concluded that inhomogeneous and discontinuous grain growth was responsible for the lower quality factor of $MgWO_4$.[16] On the other hand, Choi *et al.* reported $AMoO_4$ (A: Mg, Zn and Mn) compounds with wolframite structure that possess more than 95% theoretical density and explained the variation in quality factor of these compounds in terms of the ionic radius of A-site cation.[18] Correlation among sintering temperature, quality factor and atomic packing fraction was reported by Liao *et al.* in $ZnTiNbTaO_8$ compound where they showed that the

compound with higher packing factor possessed higher quality factor.[42]

In addition to these structural parameters, the presence of localized 3d electrons in the constituent ions induces conductivity which in turn influences the quality factor of the compounds.[41] In this view, researchers investigated the correlation among the quality factor and localized 3d electrons present in the constituent ions in compounds with perovskite and columbite crystal structure.[41,43] The variation in quality factor of $A^{2+}TiO_3$ (A: Ni, Mg and Mn) compounds was explained by the presence of localized 3d electrons in divalent metal ions and it was concluded that the presence of localized 3d electrons in Ni^{2+} ($3d^8$) and Mn^{2+} ($3d^5$) was responsible for their lower quality factor in comparison with Mg^{2+} ($3d^0$) substituted compound.[43] In a similar way, Lee *et al.* correlated the variation in quality factor of MNb_2O_6 (M: Ca, Mn, Co and Zn) compounds with columbite structure with the localized 3d electrons present in the ions.[41] Recently, Kim *et al.* reported the microwave dielectric properties of ABO_4 (A: Ni, Mg, Zn; B: W, Mo) compounds with wolframite crystal structure where they observed an interesting correlation among atomic packing fraction and quality factor of all these compounds except $NiWO_4$ and explained its lower quality factor by localized 3d electrons which induce conductivity in $NiWO_4$.[20]

In the present studies on $Ni_{1-x}(Zn_{1/2}Zr_{1/2})_xW_{1-x}Nb_xO_4$ (x = 0.0–1.0) compounds, as we mentioned in the discussion of the powder X-ray diffraction analysis, the unit cell volume increases with increasing x which in turn decreases the packing fraction of these compounds according to eqn (8) given below.[14] We have calculated the packing fraction of all these compounds and the values are given in Table 6. With increasing x, we observed an enhancement in quality factor of $Ni_{1-x}(Zn_{1/2}Zr_{1/2})_xW_{1-x}Nb_xO_4$ (x = 0.0–1.0) compositions in spite of their lower packing factor values which is clearly shown in Fig. 14. This contradictory behaviour in quality factor of these compositions is explained by localized 3d electrons present in the constituent ions. When moving from Ni^{2+}-rich compounds to Ni^{2+}-poor compounds, the conductivity of the compounds will decrease because of replacement of divalent metal Ni^{2+} ($3d^8$) having localized 3d electrons with empty Zr^{4+} ($4d^0$) and completely filled Zn^{2+} ($3d^{10}$) ions at A-sites of these compounds, which is confirmed by measuring the AC conductivity of all these compositions using expression (9) given below.

$$\text{Packing fraction } (\%) = \frac{\text{Volume of packed ions}}{\text{Volume of primitive unitcell}} = \frac{\text{Volume of packed ions}}{\text{Volume of unitcell}} \times Z = \frac{4\pi/3 \times ({r_A}^3 + {r_B}^3 + 4 \times {r_O}^3)}{\text{Volume of unitcell}} \times Z \quad (8)$$

where r_A, r_B and r_O represent ionic radius of A- and B-site cations and O^{2-} respectively. Z is the number of formula units per unit cell.

$$\text{AC conductivity}, \sigma_{ac} = \varepsilon' \varepsilon_0 \omega \tan\delta \quad (9)$$

where ε' and ε_0 represent the real part and free space permittivity respectively, and ω and $\tan\delta$ are the angular frequency and loss tangent of the compositions.

From the above expression, we can clearly see that the conductivity is directly proportional to the loss tangent. The measured AC conductivity values of these compositions are shown in the inset of Fig. 14 and from this we can see the decrease in AC conductivity of these compositions with increasing x which in turn decreases the losses present in the compositions, and hence the composition with lower Ni^{2+} concentration possesses higher quality factor. Therefore, enhancement in the quality factor of $Ni_{1-x}(Zn_{1/2}Zr_{1/2})_xW_{1-x}Nb_xO_4$ (x = 0.0–1.0) compositions is explained by d electrons present in the constituent ions of these compositions. The variation in quality factor of these compounds is shown in Fig. 14.

3.3.3 Temperature coefficient of resonant frequency (τ_f). The temperature coefficient of resonant frequency (τ_f) is a key parameter of any dielectric resonator material which decides the performance of dielectric resonators at different atmospheric conditions and is related to temperature coefficient of dielectric constant (τ_ε) by the following relation:

$$\tau_f = -\alpha - \frac{1}{2}\tau_\varepsilon \quad (10)$$

where α represents the coefficient of thermal expansion of these resonators, which in general is in the region of 10 ppm $°C^{-1}$ for all ceramic materials. As α is very low, the variation of τ_f predominantly depends on temperature coefficient of dielectric constant (τ_ε). From the Clausius–Mosotti equation one can obtain τ_ε as given below:[44]

$$\tau_\varepsilon = \frac{1}{\varepsilon}\left(\frac{\partial\varepsilon}{\partial T}\right) = \frac{(\varepsilon-1)(\varepsilon+2)}{\varepsilon}(A+B+C) \quad (11)$$

$$A = -\frac{1}{3V}\left(\frac{\partial V}{\partial T}\right)_P \quad B = \frac{1}{3\alpha_m}\left(\frac{\partial \alpha_m}{\partial V}\right)_T\left(\frac{\partial V}{\partial T}\right)_P \quad C = \frac{1}{3\alpha_m}\left(\frac{\partial \alpha_m}{\partial T}\right)_V$$

where α_m and V represent the polarizability and volume of macroscopic small sphere respectively.

According to Bosman and Havinga,[44] the first two terms A and B are related to the volume expansion with increasing the temperature which have nearly equal magnitude and opposite sign; therefore the effect of A and B on τ_ε is negligible. The third term C gives the restoring force acting on the ions and this restoring force depends on the shape of the potential well. Hence the term C is explained by the structural parameters such as octahedral distortions in the compounds.

An invar cavity attached to a programmable hot plate was used to measure the temperature coefficient of resonant frequency (τ_f) of $Ni_{1-x}(Zn_{1/2}Zr_{1/2})_xW_{1-x}Nb_xO_4$ (x = 0.0–1.0) compositions and the values are given in Table 6. Fig. 15 shows the variation of τ_f of $Ni_{1-x}(Zn_{1/2}Zr_{1/2})_xW_{1-x}Nb_xO_4$ (x = 0.0–1.0) compositions, and from this we can see that, with increasing x, the τ_f values varied from −26 ppm $°C^{-1}$ to −49 ppm $°C^{-1}$. As the temperature coefficient of resonant frequency depends on the structural characteristics of materials, Kim *et al.* reported[19] the variation of τ_f with the average octahedral distortion in $ATiO_3$,

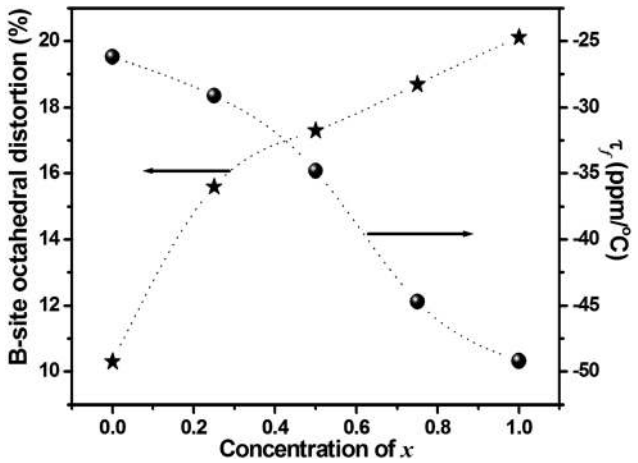

Fig. 15 Correlation among B-site octahedral distortion and temperature coefficient of resonant frequency of $Ni_{1-x}(Zn_{1/2}Zr_{1/2})_xW_{1-x}Nb_xO_4$ compositions.

ATa_2O_6 and AWO_4 (A: Ni, Mg and Co) compositions. With increasing octahedral distortion, the restoring forces between the cation and oxygen will increase which indirectly influences the temperature coefficient of resonant frequency of these compounds.[19] A similar analysis was reported by Kim *et al.* for $(Zn_{1/3}B_{2/3}{}^{5+})_xTi_{1-x}O_2$ (B: Nb, Ta) with rutile structure,[45] where the deviation of τ_f from zero is explained by the increase in the octahedral distortion of the compounds. In $Ni_{1-x}(Zn_{1/2}Zr_{1/2})_xW_{1-x}Nb_xO_4$ compounds, substitutions of higher ionic radius[22] elements Zn^{2+} (0.74 Å), Zr^{4+} (0.72 Å) and Nb^{5+} (0.69 Å) influence the cation–oxygen bond lengths and resulting in an increase in the $(Nb/W)O_6$ octahedral distortion from 10% to 20% which in turn deviates τ_f away from zero, *i.e.* −26 ppm $°C^{-1}$ to −49 ppm $°C^{-1}$. Hence, the variation in τ_f of $Ni_{1-x}(Zn_{1/2}Zr_{1/2})_xW_{1-x}Nb_xO_4$ (x = 0.0–1.0) compositions is explained by B-site octahedral distortion and is shown in Fig. 15.

4. Conclusions

We have successfully synthesized $Ni_{1-x}(Zn_{1/2}Zr_{1/2})_xW_{1-x}Nb_xO_4$ (x = 0.0–1.0) compositions *via* a conventional solid-state reaction method and observed them to possess monoclinic wolframite crystal structure with *P*2/*c* space group. The splitting in the powder X-ray diffractograms of these compounds is explained with the lattice parameter by calculating *d*-spacing values of (−111) and (111) reflections of these compounds. The additional Raman modes appearing in the spectra of Zn^{2+}, Zr^{4+} and Nb^{5+} substituted compositions are explained by the electronegativity difference between the cations (Nb and W) at B-sites of these compositions whereas the variation in the FWHM and intensity of Raman modes is attributed to the presence of randomly distributed multiple cations (Ni^{2+}, Zn^{2+} and Zr^{4+} at A-sites and Nb^{5+}, W^{6+} at B-sites) at a particular site. XPS analysis reveals that all the elements are in their respective oxidation state in these compositions. Increase in grain size was observed when moving from Ni^{2+}-rich compositions to Ni^{2+}-poor composition which is clearly seen from the scanning electron micrographs of these compositions. All the compositions possess more than 95% theoretical density with good microwave dielectric properties (ε_r ~ 12–15, $Q \times f$ ~ 23 500–53 000 GHz and τ_f ~ −25 ppm $°C^{-1}$ to −49 ppm $°C^{-1}$). The enhancement in dielectric constant and quality factor of these compositions is correlated with polarizability and 3d electrons present in the constituent ions of the respective compositions. The variation in τ_f is explained by an increase in the B-site octahedral distortion in these compositions.

Acknowledgements

The authors are grateful to the University Grant Commission, New Delhi, India for providing financial assistance in the form of a Senior Research Fellowship. The authors especially thank Prof. S. Ramaprabhu and Prof. B. Viswanathan for allowing the use of the X-ray photoelectron spectroscopy instrument. The authors thank Ashok P, Department of Physics, IIT Madras for his cooperation in doing XPS measurements.

References

1 R. J. Cava, *J. Mater. Chem.*, 2001, **11**, 54.
2 I. M. Reaney and D. Iddles, *J. Am. Ceram. Soc.*, 2006, **89**, 2063.
3 M. T. Sebastian, *Dielectric materials for wireless communication*, Elsevier publishing group, 2008.
4 H. Zheng, G. D. C. de Fyorgyfalva and I. M. RANEY, *J. Mater. Sci.*, 2005, **40**, 5207.
5 C.-F. Tseng, C.-L. Huang, N.-R. Yang and C.-H. Hsu, *J. Am. Ceram. Soc.*, 2006, **89**, 465.
6 H. Yamada, T. Okawa, Y. Yohdo and H. Ohsato, *J. Eur. Ceram. Soc.*, 2006, **26**, 2059.
7 H.-J. Lee, I.-T. Kim and K. S. Hong, *Jpn. J. Appl. Phys.*, 1997, **36**, L1318.
8 G.-K. Choi, S.-Y. Cho, J.-S. An and K. S. Hong, *J. Eur. Ceram. Soc.*, 2006, **26**, 2011.
9 G.-K. Choi, J.-R. Kim, S. H. Yoon and K. S. Hong, *J. Eur. Ceram. Soc.*, 2007, **27**, 3063.
10 E. S. Kim, S.-H. Kim and B. I. Lee, *J. Eur. Ceram. Soc.*, 2006, **26**, 2101.
11 D. Zhou, W.-B. Li, L.-X. Pang, J. Guo, Z.-M. Qi, T. Shao, X. Yao and C. A. Randall, *Dalton Trans.*, 2014, **43**, 7290.
12 D. Zhou, L.-X. Pang, J. Guo, Z.-M. Qi, T. Shao, X. Yao and C. A. Randall, *J. Mater. Chem.*, 2012, **22**, 21412.
13 M. Daturi, G. Busca, M. M. Borel, A. Leclaire and P. Piaggio, *J. Phys. Chem. B*, 1997, **101**, 4358.
14 E. S. Kim, B. S. Chun, R. Freer and R. J. Cernik, *J. Eur. Ceram. Soc.*, 2010, **30**, 1731.
15 S. H. Yoon, D. W. Kim, S. Y. Cho and K. S. Hong, *J. Eur. Ceram. Soc.*, 2006, **26**, 2051.

16 R. C. Pullar, S. Farrah and N. M. Alford, *J. Eur. Ceram. Soc.*, 2007, **27**, 1059.
17 R. D. Shannon, *J. Appl. Phys.*, 1993, **73**, 348.
18 G. K. Choi, J. R. Kim, S. H. Yoon and K. S. Hong, *J. Eur. Ceram. Soc.*, 2007, **27**, 3063.
19 E. S. Kim and C. J. Jeon, *Applications of Ferroelectrics*, *ISAF 2009*, 2009, p. 1.
20 E. S. Kim, C. J. Jeon and P. G. Clem, *J. Am. Ceram. Soc.*, 2012, **95**, 2934.
21 A. C. Larson and R. B. von Dreele, *General Structural Analysis System (GSAS)*, Los Alamos National Laboratories, Los Alamos, NM, 1990.
22 B. H. Toby, *J. Appl. Crystallogr.*, 2001, **34**, 210.
23 B. W. Hakki and P. D. Coleman, *IRE Trans. Microwave Theory Tech.*, 1960, **8**, 402.
24 R. D. Shannon, *Acta Crystallogr., Sect. A: Cryst. Phys., Diffr., Theor. Gen. Cryst.*, 1976, **32**, 751.
25 A. S. Barker Jr., *Phys. Rev.*, 1964, **135**, A742.
26 S. P. S. Porto and J. F. Scott, *Phys. Rev.*, 1967, **157**, 716.
27 M. G. Thube, S. K. Kulkarni, D. Huerta and A. S. Nigavekar, *Phys. Rev. B*, 1986, **34**, 6874.
28 A. Maione and M. Devillers, *J. Solid State Chem.*, 2004, **177**, 2339.
29 G. P. Halada and C. R. Clayton, *J. Vac. Sci. Technol., A*, 1993, **11**, 2342.
30 M. N. Mancheva, R. S. Iordanova, D. G. Klissurski, G. T. Tyuliev and B. N. Kunev, *J. Phys. Chem. C*, 2007, **111**, 1101.
31 R. D. Seals, R. Alexander, L. T. Taylor and J. G. Dillard, *Inorg. Chem.*, 1973, **12**, 2485.
32 L. G. Mar, P. Y. Timbrell and R. N. Lamb, *Thin Solid Films*, 1993, **223**, 341.
33 T. H. Boyuklimanli and J. H. Simmons, *J. Non-Cryst. Solids*, 1989, **120**, 262.
34 K. F. Dong, H. H. Li, Y. G. Peng, G. Ju, G. M. Chow and J. S. Chen, *Sci. Rep.*, 2014, 4.
35 D. D. Sarma and C. N. R. Rao, *J. Electron Spectrosc. Relat. Phenom.*, 1980, **20**, 25.
36 M. H. Liang, C. T. Hu, H. F. Cheng, I. N. Lin and J. Steeds, *J. Eur. Ceram. Soc.*, 2001, **21**, 2759.
37 W. S. Kim, E. S. Kim and K. H. Yoon, *J. Am. Ceram. Soc.*, 1999, **82**, 2111.
38 S. R. Kiran, G. Sreenivasulu, V. R. K. Murthy, V. Subramanian and B. S. Murthy, *J. Am. Ceram. Soc.*, 2012, **95**, 1973.
39 X. C. Fan, X. M. Chen and X. Q. Liu, *Chem. Mater.*, 2008, **20**, 4092.
40 N. Ichinose and T. Shimada, *J. Eur. Ceram. Soc.*, 2006, **26**, 1755.
41 H.-J. Lee, K.-S. Hong and S.-J. Kim, *Mater. Res. Bull.*, 1997, **32**, 847.
42 Q. Liao, L. Li, X. Ren and X. Ding, *J. Am. Ceram. Soc.*, 2011, **94**, 3237.
43 J.-H. Sohn, Y. Inaguma, S.-O. Yoon, M. Itoh, T. Nakamura, S.-J. Yoon and H.-J. Kim, *Jpn. J. Appl. Phys.*, 1994, **33**, 5466.
44 A. J. Bosman and E. E. Havinga, *Phys. Rev.*, 1963, **129**, 1593.
45 E. S. Kim and D. H. Kang, *Ceram. Int.*, 2008, **34**, 883.